RSC Advances

PAPER

View Article Online
View Journal | View Issue

Cite this: *RSC Adv.*, 2023, **13**, 16327

Characterization of cellulose-functionalized phillipsite biocomposite as an enhanced carrier of oxaliplatin drug during the treatment of colorectal cancer: loading, release, and cytotoxicity

Haifa E. Alfassam,[a] Menna-Tullah Ashraf,[bc] Sarah I. Al Othman,[a] Maha A. Al-Waili,[a] Ahmed A. Allam[d] and Mostafa R. Abukhadra *[ce]

Natural phillipsite (N.Ph) was hybridized with cellulose fibers to produce a safe biocomposite (CF/N.Ph) as an enhanced delivery structure of traditional oxaliplatin (OXPN) chemotherapy during the treatment stages of colorectal cancer cells. The requirements of CF/N.Ph as a carrier for OXPN were followed based on the loading, release, and cytotoxicity compared to N.Ph. CF/N.Ph composite exhibits a notably higher OXPN encapsulation capacity (311.03 mg g^{-1}) than the N.Ph phase (79.6 mg g^{-1}). The OXPN encapsulation processes into CF/N.Ph display the isotherm behavior of the Freundlich model (R^2 = 0.99) and the kinetic assumptions of pseudo-first order kinetic (R^2 > 0.95). The steric studies reflect a strong increment in the quantities of the free sites after the cellulose hybridization steps (Nm = 100.01 mg g^{-1}) compared to pure N.Ph (Nm = 27.94 mg g^{-1}). Additionally, the capacity of each site was enhanced to be loaded by 4 OXPN molecules (n = 3.11) compared to 3 by N.Ph (n = 2.85) in a vertical orientation. The OXPN encapsulation energy into CF/N.Ph (<40 kJ mol^{-1}) reflects physical encapsulation reactions involving electrostatic attraction, van der Waals forces, and hydrogen bonding. The OXPN release profiles of CF/N.Ph exhibit slow and controlled properties for about 150 h either at pH 5.5 or at pH 7.4. The release kinetics and diffusion exponent (>0.45) signify non-Fickian transport and a complex erosion/diffusion release mechanism. The free CF/N.Ph particles display a considerable cytotoxic effect on HCT-116 cancer cells (46.91% cell viability), and its OXPN-loaded product shows a strong cytotoxic effect (3.14% cell viability).

Received 4th April 2023
Accepted 9th May 2023

DOI: 10.1039/d3ra02243a

rsc.li/rsc-advances

1 Introduction

Non-contagious diseases, mainly the most widely distributed species of cancer, are classified as the most lethal to human beings. 72% of the documented fatalities in the contemporary world are significantly related to common non-contagious diseases.[1,2] Among the reported types of cancer, the colorectal type has been recognized as an extensively distributed malignancy that exhibits strong adverse impacts on the gastrointestinal tract.[3,4] About 13% of the documented cancer diseases in the world are colorectal cancer; therefore, it was classified as one of the dominant causes of death and an uncontrolled increase in the mortality rate recently.[5,6] Therefore, the development of effective therapies that can inhibit the tumor cells of colorectal cancer at a low cost and significant rate without strong side effects became the main focus points of the health authorities as well as the interested scientific communities.[7,8]

Therefore, different species and forms of chemotherapies have been evaluated as effective anticancer agents with promising inhibition impacts on the activity and progressive spread of the target tumor cells.[9,10] The most commonly used anticancer therapies depend on their capacities to form significant oxidative stresses that can inhibit replication of the DNA of the tumor cells and, finally, their death.[7,11] Unfortunately, the controlled release and the several dosages of most of the used chemotherapies are associated with remarkable toxic and adverse health impacts on the fresh cells, such as bone marrow suppression, damage to the kidney, and nausea.[4,12] Therefore, several studies have been developed and introduced to enhance the biocompatibility, selectivity, safety, and therapeutic influences of commercially used chemotherapies.[4] This enhancement has been suggested to be performed either by the production of innovative new types of anticancer therapies or by

[a]*Princess Nourah bint Abdulrahman University, College of Science, Biology Department, Riyadh, Saudi Arabia*
[b]*Chemistry Department, Faculty of Science, Beni-Suef University, Beni-Suef, 65211, Egypt*
[c]*Materials Technologies and their Applications Lab, Geology Department, Faculty of Science, Beni-Suef University, Beni-Suef City, Egypt. E-mail: Abukhadra89@Science.bsu.edu.eg*
[d]*Zoology Department, Faculty of Science, Beni-Suef University, Beni-Suef, Egypt*
[e]*Geology Department, Faculty of Science, Beni-Suef University, Beni-Suef, 65211, Egypt*

inducing the activity and biosafety of commercially used traditional types.[3]

Oxaliplatin (OXPN) drug is one of the commercially used chemotherapies permitted by the FAD organization to be applied as a highly effective anticancer drug, especially during the metastatic phases of tumor cells.[3,11,12] Chemically, the structure of OXPN produces numerous quantities of platinum base reactive complexes that characterize significant inhibition properties against the DNA of tumor cells.[3,11] However, the poor solubility of OXPN as a chemical compound in the bloodstream and the strong pernicious properties of its metabolite qualities on fresh organs and tissues set strong restrictions on their applications and dosages.[5,7,13] Moreover, nausea, GI tract abnormalities, digestive difficulties, neurotoxicity, cardiotoxicity, and myelotoxicity have been documented as common health drawbacks during the treatment periods using OXPN.[5,9,11] Several potential techniques have been suggested to enhance the therapeutic, solubility, safety, and selectivity properties of OXPN chemotherapies in addition to their curative value and release rate within human organs.[7,13] The trapping or supporting of the OXPN molecules into advanced carriers or structures as advanced delivery systems was introduced as an enhancement technique that can be recommended to regulate the delivered dosages of the drug according to certain intervals and controlled rates to avoid common side effects and expand the interaction duration.[10,13]

Several species of organic, inorganic, and hybrid organic/inorganic materials were investigated as potential carriers and delivery systems of OXPN, which strongly enhanced its retention and permeation properties.[10,14,15] The studied structures as carriers involved kaolinite, bentonite/cellulose composite, alginate, mesoporous silica, lipid nanoparticles, synthetic polymers, and liposomes.[6,7,10,12,13,16] Different species of natural zeolite and their based composites and modified products have attracted the attention of scientific communities as pharmaceutical materials and promising biocompatible delivery systems.[17,18] The commonly tested natural zeolite forms display remarkably significant textural and physicochemical properties (such as surface area, porosity, surface reactivity, thermal stability, ion exchange capacity, chemical stability, and adsorption capacity), in addition to their bioavailability, biocompatibility, and safe properties.[5,19,20] However, most of the presented studies on the medical and environmental applications of natural zeolite focused on the clinoptilolite phase, and few and non-satisfy studies have been developed on other phases, such as natural phillipsite.[21,22] Natural phillipsite (N.Ph) is an essential natural zeolite mineral that is characterized by significant natural reserves and comprises hydrated aluminum-silicate units with tetrahedral geometry.[23] However, phillipsite, as a zeolitic material, exhibits significant safety and biocompatibility; its hydrophilic surface strongly decreases its encapsulation capacities as carriers of drug organic molecules that are of a high ionic radius.[22] The organic surface modification and polymeric functionalization of phillipsite can induce its oragophilicity significantly in addition to the expected impact on its pore size distribution, which might enhance its loading and release performance as potential carriers of commonly used drugs, such as OXPN.[24,25] Moreover, hybridization using biopolymers, such as cellulose, chitosan, and β-cyclodextrin, can strongly induce the biocompatibility, biodegradability, and therapeutic effects of the obtained structure.[12,18,26,27]

Therefore, this study aims to develop hybridized and functionalized phillipsite particles with cellulose fibers as a hybrid structure (CF/N.Ph) of enhanced physicochemical, biocompatible, and anticancer properties during its assessment as a low-cost and effective delivery system of oxaliplatin drug (OXPN). The cellulose fibers were selected as functionalized polysaccharide biopolymers owing to their availability as a natural-based product characterized by significant surface reactivity, non-toxicity, thermal stability, biodegradability, chemical stability, and biocompatibility.[24,28,29] The properties of natural phillipsite (N.Ph) and its cellulose functionalized product (CF/N.Ph) and potential delivery structures of OXPN molecules were investigated in detail for the first time based on encapsulation behaviors, release profiles, and cytotoxic impacts on colorectal cancer cells (HCT-116). Moreover, the affecting mechanisms during the encapsulation and release processes were illustrated based on kinetic and equilibrium studies.

2 Experimental work

2.1. Materials

Natural zeolite (phillipsite (N.Ph)) was obtained as raw samples from the mines of natural zeolite in the Mukeihlat area, Syria. The cellulose fibers, which were used during the functionalization reactions, are microcrystalline cellulose of analytical grade (Sigma-Aldrich; Egypt) in addition to dimethyl sulfoxide (DMSO) (CAS: 67-68-5; >99.5%; Sigma-Aldrich) as dissolving reagent. A commercial oxaliplatin drug with [SP-4-2-(1*R-trans*)]-(1,2-cyclohexanediamine-*N*,*N*′) [ethanedioata(2-)-*O*,*O*′] platinum chemical structure and 397.29 MW was used to study the loading, release, and cytotoxic properties of the structures as delivery systems and was obtained from Sigma-Aldrich Company, Egypt.

2.2. Synthesis of cellulose-functionalized phillipsite (CF/N.Ph)

The functionalization of the phillipsite with the cellulose fibers was performed based on the reported method by Altoom *et al.*[12] 2 g of phillipsite particles were homogenized within distilled water (50 mL) for 120 min using a complex mixing system that involves a magnetic stirrer (500 rpm) supplied with a sonication source (240 W). As a parallel process, 1 g of the cellulose fibers was dispersed within 50 mL of DMSO for 24 h by stirring at 500 rpm, and homogenization was induced after that by the sonication step for 120 min. The obtained cellulose suspension was added to the phillipsite suspension under continuous homogenization processes for 24 h using both a magnetic stirrer (500 rpm) and sonication irradiation (240 W). Then, the obtained CF/N.Ph composite particles were extracted from the residual solution by a centrifugation process at 3500 rpm for 15 min, washed several times to neutralize the surface of the composite, and dried for 24 h at 60 °C.

2.3. Analytical techniques

The crystalline phases and the structural properties during the synthesis procedures were determined according to the X-ray diffraction patterns obtained by a PANalytical-Empyrean X-ray diffractometer within the determination range of 0–70°. The essential chemical and integrated groups during the functionalization steps were identified based on the FT-IR spectra of the prepared structures using a Fourier Transform Infrared spectrometer (FTIR-8400S; Shimadzu) within an estimation range of 400–4000 cm^{-1}. The surficial morphologies and their changes in the modification procedures were inspected based on SEM images of the synthetic materials using a Scanning Electron Microscope (Gemini, Zeiss-Ultra 55). Texturally, the surface area and porosity properties were evaluated based on the obtained N_2 adsorption/desorption isotherm curves of the raw and prepared materials by applying a surface area analyzer (Beckman Coulter SA3100).

2.4. OXP encapsulation studies

The encapsulating studies of OXPN into both N.Ph and CF/N.Ph were evaluated based on the fundamentally investigated factors to control the OXPN encapsulated dosage in addition to the maximum encapsulation capacities. The assessed factors are the pH (2–9), encapsulation duration (1 h to 24 h), OXPN concentration (100–800 mg L^{-1}), and temperature (20–50 °C). The N.Ph and CF/N.Ph particles were homogenized effectively within the prepared OXPN solutions (50 mL) using a vortex rotator. After the equilibration period of each encapsulation test, the N.Ph and CF/N.Ph particles were removed from the solutions by filtration utilizing Whatman filter paper, and the remaining OXPN concentrations in the solutions were measured by applying a UV-Vis spectrophotometer at a fixed determination wavelength (λ(max) = 209 nm). The determined remaining OXPN concentrations were applied to calculate the encapsulation capacities of N.Ph and CF/N.Ph particles in mg g^{-1} according to eqn (1). The performed OXPN encapsulation tests into N.Ph and CF/N.Ph particles were accomplished in triplicated forms, and the estimated average values were presented in the studies with standard deviations < 3.7%.

$$\text{Capacity}\left(\text{mg g}^{-1}\right) = \frac{(\text{Initial concentration} - \text{residual concentration}) \times \text{solvent volume}}{\text{Carrier weight}}$$

2.5. Release studies

The OXPN release profiles of the N.Ph and CF/N.Ph particles were evaluated within two types of chemical buffers (phosphate buffer (pH 7.4) and acetate buffer (pH 5.5)) considering the experimental temperature of 37.5 °C. The OXPN encapsulated N.Ph and CF/N.Ph particles (100 mg g^{-1}) were carefully dispersed separately within 500 mL of the prepared chemical release buffers. The homogenization processes between the OXPN-loaded N.Ph and CF/N.Ph particles and the two buffers were accomplished by employing a DISTEK dissolution apparatus for 120 h at 200 rpm as the rotation speed of the vessels. Samples of the two buffers (5 mL) were extracted regularly from the bulk release solutions at specific time intervals to follow the percentages of the diffused OXPN molecules from the N.Ph and CF/N.Ph particles using a UV-Vis spectrophotometer at a fixed determination wavelength (λ(max) = 209 nm). The regularly obtained samples during the release tests of OXPN from the N.Ph and CF/N.Ph particles were readded immediately after the measurements to the bulk release buffers to maintain the volume at the same values throughout the investigated total investigated release period. The performed OXPN release tests into N.Ph and CF/N.Ph particles were accomplished in triplicated forms, and the estimated average values were presented in the studies considering eqn (2) to determine the release percentages with standard deviations <4.2%:

$$\text{OXPN release}(\%) = \frac{\text{The amount of released OXPN}}{\text{Amount of oaded OXPN}} \times 100 \quad (2)$$

2.6. *In vitro* cytotoxicity

2.6.1. Cell lines. The anti-cancer and cytotoxicity properties of free N.Ph and CF/N.Ph particles and their OXPN loading samples were evaluated against fresh colorectal and colorectal cancer cells. The tests were conducted at the Regional Center for Microbiology and Biotechnology, Al-Azhar University, Egypt. The incorporated chemicals and reagents during the tests were Gentamycin, colorectal malignant cell lines (HCT-116) (American Type Culture Collection), 0.25% trypsin–EDTA, dimethyl sulfoxide (DMSO), RPMI-1640, DMEM, fetal bovine serum, HEPES buffer, and 3 (4,5-dimethylthiazol-2-yl)-2.5 diphenyltetrazolium bromide (MTT 99%).

2.6.2. *In vitro* cytotoxicity. The cancer cell lines (HCT-116) were first immersed carefully in RPMI-1640 as the incorporated culturing medium under specific conditions of temperature (37 °C) and an inert atmosphere (5% CO_2). Afterward, the incorporated culturing medium was significantly supplemented with gentamycin (50 μg mL^{-1}) in addition to fetal calf serum (10%). The previously reported procedures were repeated carefully three times per week; then, the HCT-116 cell lines (5×10^4 cell per well) were immersed for 24 h within specific Corning®96-well plates. After that, the free N.Ph and CF/N.Ph particles and their OXPN loading samples were homogenized with the cell lines in a series of separated tests and incubated for 24 h. During this period, the generated viable cells were measured based on the criteria of the MTT cell proliferation assay. By the end of the incubation process (after 24 h), the previously incorporated culturing medium was removed and

replaced immediately with a mixture of 100 μL of fresh RPMI medium and 10 μL of MTT (12 mM). This mixture was incubated for 5 h, and the generated purple formazan during this incubation was dissolved by DMSO (50 μL). The optical density of the treated HCT-116 cell lines either by the free N.Ph and CF/N.Ph particles or their OXPN loading samples was measured using a microplate at 590 nm as the measuring wavelength. The measured values were applied directly to calculate the cell viability percentage as follows:

$$\text{Cell viability}(\%) = \frac{\text{Mean OD}}{\text{Control OD}} \times 100 \quad (3)$$

3 Results and discussion

3.1. Characterization of the carriers

3.1.1. XRD analysis. The XRD patterns were evaluated to detect the present crystalline phases and the structural impacts of the integration reactions. The diffraction pattern of the raw sample displays the characteristic peaks of well crystalline phillipsite (natural zeolite) at 2 Theta angles of 12.32°, 17.59°, 21.54°, 26.0°, 27.95°, 29.43°, 33.20°, 45.84°, and 60.5° (Fig. 1A).[30] The observed pattern of the integrated cellulose fibers as pure phase reflects its crystalline nature with common peaks of commercial cellulose at 14.6° (1$\bar{1}$0), 16.62° (110), 22.7° (200), and 34.6° (004) (JCPDS card no 00-056-1718) (Fig. 1B). The recognized diffraction pattern of phillipsite after the functionalization process with cellulose confirms the significant interaction and integration between them (Fig. 1C). The characteristic peaks of cellulose (16.65° and 22.5°) were identified clearly in addition to the essential peaks of phillipsite (12.39°, 26.09°, 27.95°, 29.47°, and 33.4°) that deviated from their original sites, and their intensities declined at a considerable rate in addition to the marked disappearance of some peaks (Fig. 1C). The previous observations demonstrated the successful integration of the cellulose chains either by grafting the cellulose chains within the structural pores of zeolite or by the formation of chemical complexes between them.

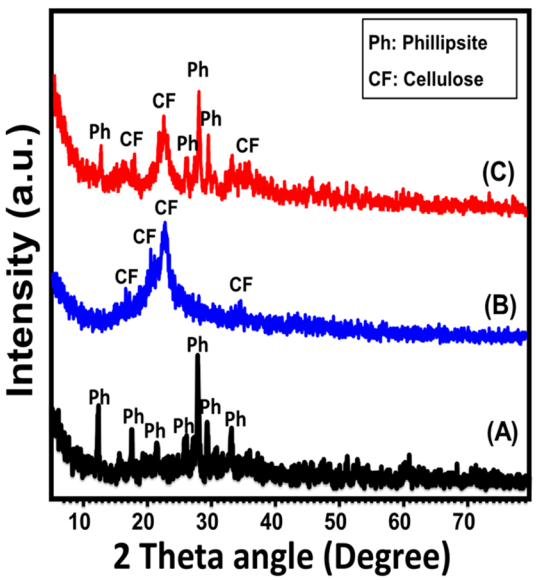

Fig. 1 XRD patterns of natural phillipsite (A), cellulose fibers (B), and synthetic CF/N.Ph composite (C).

3.1.2. SEM analysis. The SEM images were used to illustrate the morphological features of the synthetic composite and the nature of the integration procedures (Fig. 2). The phillipsite as a raw sample appeared in an agglomerated and massive form, which is disseminated with several grains of high crystalline nature and well-developed prismatic shape that characterize the natural morphology of phillipsite (Fig. 2A). Regarding the synthetic CF/N.Ph composite, the observed particles reflected significant decoration of the cellulose fibers with the phillipsite grains at random orientation (Fig. 2B–D). Moreover, the interaction between the phillipsite grains and cellulose gives the composite particle rugged topography in addition to new morphological features. The new morphological features were marked by the intersection of the cellulose fibers at random orientations producing flower-like forms (Fig. 2D), which significantly affect the surface area of the obtained structure. This significantly induced the determined surface area of the CF/N.Ph composite to be 264.2 $m^2\ g^{-1}$ compared to 216 $m^2\ g^{-1}$ for raw phillipsite.

3.1.3. FT-IR analysis. The impact of the functionalization and hybridization of phillipsite with cellulose, in addition to the encapsulation effect of OXPN, was investigated based on the dominant chemical groups according to the FT-IR spectra of the evaluated material (Fig. 3). The essential absorption bands of the FT-IR spectrum of raw phillipsite clearly signify the functional groups of natural zeolites, such as Si–O–Al (449 cm^{-1}), Si–O (708 cm^{-1}), Si–O–Si (1023 cm^{-1}), trapped water within the zeolite channels (1434 cm^{-1}), and Si–OH (3437 cm^{-1})[31] (Fig. 3A). The spectrum of the cellulose/phillipsite hybridized structure was addressed compared with the spectrum of the pure phase of cellulose fibers. The spectrum of separated cellulose fibers clearly demonstrates the bands of the structural organic groups, such as –CH bearing chemical groups (2914 and 1367 cm^{-1}), –C–O–C bonds within the pyranose rings (1057 cm^{-1}), and the β-glycosidic linkages (897 cm^{-1})[12,32] (Fig. 3B).

The spectrum of CF/N.Ph composite exhibits clearly complex properties involving the marked spectrum bands of the organic structure of cellulose and spectrum bands of the inorganic aluminosilicate structure of phillipsite (Fig. 3C). The detected chemical groups of phillipsite are Si–O–Al (448 cm^{-1}), Si–O (671 cm^{-1}), Si–O–Si (1033.7 cm^{-1}), trapped water within the zeolite channels (1438.8 cm^{-1}), and Si–OH (3359 cm^{-1}) (Fig. 3C). The identified chemical groups of cellulose in the spectrum of CF/N.Ph composite are the –CH bearing chemical groups (2900 and 1369 cm^{-1}) (Fig. 3C). The previously identified hybrid organic/inorganic chemical groups in addition to the considerable fluctuation in the positions of their identification bands validate the effective integration between cellulose and phillipsite in composite and the considerable chemical interaction between their reactive functional groups. The spectrum of the OXPN encapsulated CF/N.Ph composite exhibits

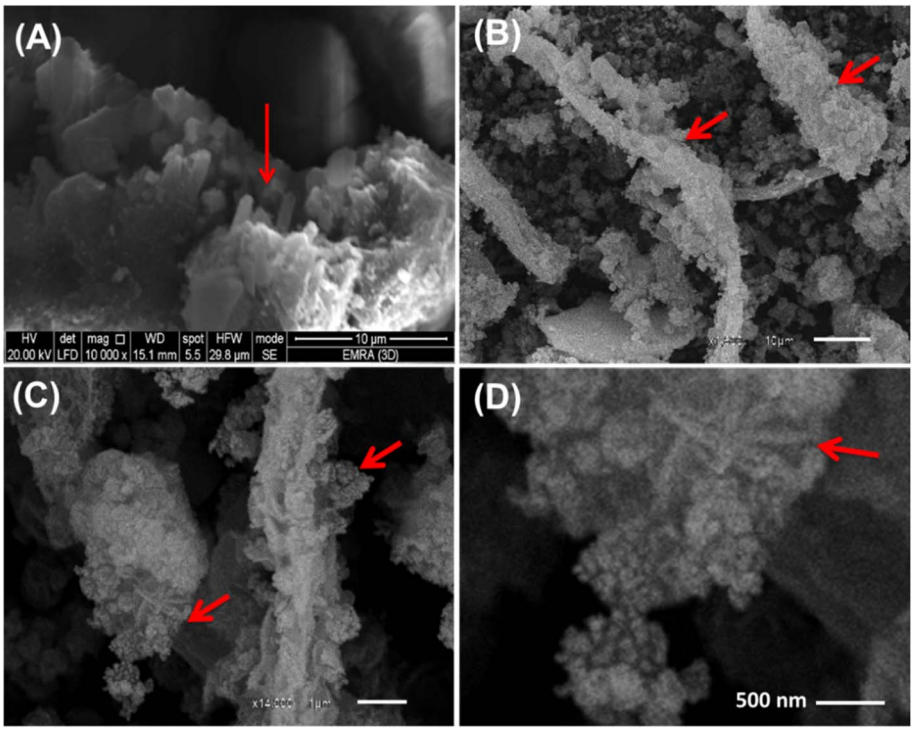

Fig. 2 SEM images of (A) natural phillipsite (red arrows refer to the prismatic crystals of phillipsite), (B) and (C) synthetic CF/N.Ph composite (red arrows refer to the decoration of the cellulose grains with the phillipsite grains), and (D) intersection of the cellulose fibers producing a flower-like form.

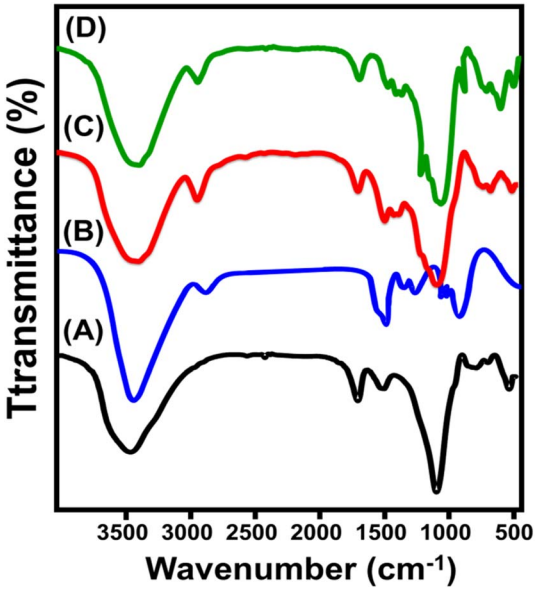

Fig. 3 FT-IR spectra of natural phillipsite (A), cellulose fibers (B), synthetic CF/N.Ph composite (C), and OXPN encapsulated CF/N.Ph composite (D).

observable shifting in the previously described bands of the present organic/inorganic chemical groups (Fig. 3D). Additionally, there is an appearance of new two bands related to the symmetric (821 cm^{-1}) and asymmetric (1293.2 cm^{-1}) stretching of Pt–O within the structure of the OXPN drug, signifying the effective trapping and encapsulation of the drug molecules within the structure of CF/N.Ph composite[7,33,34] (Fig. 3D).

3.2. Encapsulation of the OXPN drug

3.2.1. Influence of encapsulation parameters

3.2.1.1. Effect of pH. The experimental impact of the solution's pH on the achieved encapsulation capacities by both raw phillipsite (N.Ph) and the synthetic CF/N.Ph composite was followed within a tested range from pH 2 to 9 at adjusted values of the other affecting variables [OXPN concentration: 200 mg L^{-1}; dosage: 20 mg; temperature: 20 °C; duration: 4 h; and volume: 50 mL]. The experimentally detected encapsulation of OXPN into N.Ph and CF/N.Ph exhibits remarkable enhancement while performing the tests at high pH conditions (Fig. 4A). This can be detected from pH 2 (N.Ph (2.3 mg g^{-1}) and CF/N.Ph (17.4 mg g^{-1})) to pH 9 (N.Ph (25.8 mg g^{-1}) and CF/N.Ph (125.4 mg g^{-1})) (Fig. 4A). Therefore, encapsulation reactions at the basic pH values were recommended during the loading of OXPN into both N.Ph and CF/N.Ph. Generally, the solution's pH significantly controls the ionization behavior of OXPN, a dissolved chemical compound, as well as the dominant surficial charges of N.Ph and CF/N.Ph. OXPN is characterized by significant mobility and solubility in acidic conditions, which declines its effective encapsulation properties.[12,15] Moreover, the dissolved OXPN molecules exist in two basic forms ($[Pt(dach)(H_2O)Cl]^+$ and $[Pt(dach)(H_2O)_2]^{2+}$) of positive charges at acidic pH values. Therefore, they display notable competitive

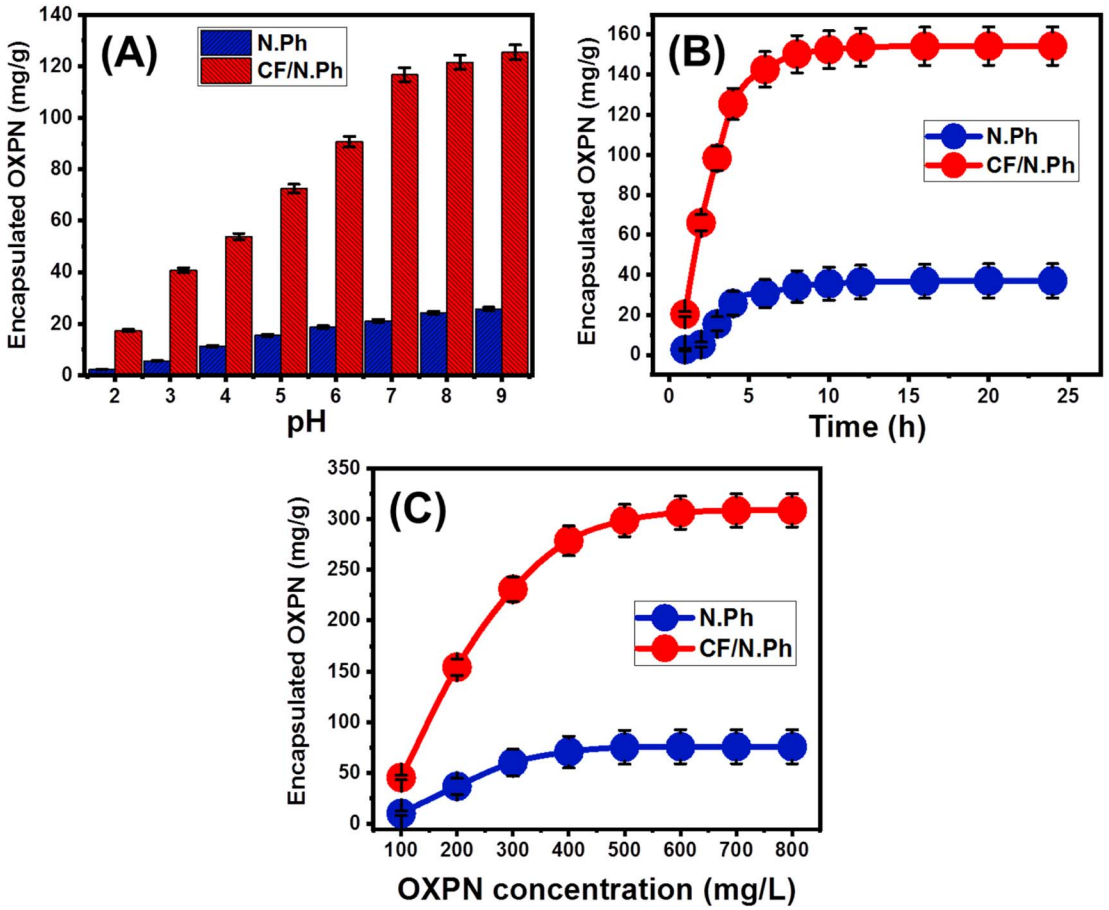

Fig. 4 Effect of the experimental factors on the OXPN encapsulation capacities of N.Ph and CF/N.Ph, including the effect of the solution pH (A), encapsulation duration (B), and OXPN initial concentration (C).

and electrostatic repulsion with hydronium ions, which are distributed extensively on the surfaces of N.Ph and CF/N.Ph.[35,36]

3.2.1.2. Encapsulation duration. The experimental impact of the encapsulation duration on the achieved capacities by both raw phillipsite (N.Ph) and the synthetic CF/N.Ph composite was followed within a tested range from 1 h to 24 h at adjusted values of the other affecting variables [OXPN concentration: 200 mg L^{-1}; dosage: 20 mg; temperature: 20 °C; pH: 9; and volume: 50 mL]. The OXPN encapsulation efficiencies of N.Ph and CF/N.Ph demonstrate remarkable enhancement in terms of both the encapsulation rates and OXPN encapsulated quantities in mg g^{-1} with regular expansion in the evaluated time interval (Fig. 4B). This enhancement impact can be signified from 1 h to 6 h in the presence of N.Ph and from 1 h to 8 h in the presence of CF/N.Ph (Fig. 4B). Afterward, the increment in the test duration exhibits no considerable impact either on the experimental rate or the OXPN encapsulated quantities, and the curves reflect stability states of nearly fixed values (Fig. 4B). Such properties signify the equilibration states of the emasculation systems of N.Ph and CF/N.Ph as potential carriers of OXPN (N.Ph (37 mg g^{-1}) and CF/N.Ph (154.3 mg g^{-1})). The existence of active encapsulation sites at their free states and extensive quantities on N.Ph and CF/N.Ph at the starting intervals of the encapsulation reactions resulted in the detected high loading rates and an abrupt increase in the OXPN encapsulated quantities.[37] The progressive encapsulation of OXPN into the existing free sites of N.Ph and CF/N.Ph with an increase in the duration of the tests causes occupation and consumption of these sites, which strongly reduces their availability. Therefore, the experimental encapsulation rate of OXPN dropped clearly after certain time intervals, and the incorporated N.Ph and CF/N.Ph particles showed ignored enhancements in the OXPN loading capacities. The loading equilibration states of N.Ph and CF/N.Ph was identified after the complete occupation of all the existing sites with the encapsulated OXPN molecules.[38]

3.2.1.3. OXPN concentration. The experimental impact of the assessed OXPN concentration on the achieved capacities by both raw phillipsite (N.Ph) and the synthetic CF/N.Ph composite was followed within a tested range from 100 to 800 mg L^{-1} at adjusted values of the other affecting variables [duration: 24 h; dosage: 20 mg; temperature: 20 °C; pH: 9; and volume: 50 mL]. The initial OXPN concentrations as an experimental variable during the loading processes are an essential factor for determining the maximum capacities of N.Ph and CF/N.Ph carriers and their equilibrium properties. Experimentally, the quantities of the encapsulated OXPN into N.Ph and CF/N.Ph increase strongly in the existence of high OXPN initial concentrations (Fig. 4C). The presence of OXPN at high concentrations

within a certain volume strongly accelerates the diffusion and mobility properties of its ions, and their driving forces increase collision chances as well as chemical interactions between the active sites of the N.Ph and CF/N.Ph solid particles and dissolved drug molecules.[39,40] This, in turn, induces the OXPN encapsulation efficiencies of N.Ph and CF/N.Ph until certain concentrations (500 mg L^{-1} (N.Ph) and 600 mg L^{-1} (CF/N.Ph)) (Fig. 4C). After testing these concentrations, any increase in the evaluated OXPN concentration exhibits neglected influence on the determined quantities of the encapsulated OXPN, which normally denote the equilibrium loading states of N.Ph and CF/N.Ph as potential carriers (Fig. 4C). Consequently, both N.Ph and CF/N.Ph attend their maximum OXPN encapsulation capacities (76 mg g^{-1} (N.Ph) and 308.5 mg g^{-1} (CF/N.Ph)). The significantly higher OXPN encapsulation capacity of CF/N.Ph than N.Ph was assigned to the following parameters: (1) reported enhancement in the surface area after the cellulose functionalization step, (2) organophilic properties of the CF/N.Ph compared to hydrophilic phillipsite, which induces its affinity to the dissolved organic molecules of OXPN, and (3) a remarkable increase in the quantities of the present and effective encapsulation sites after the integration of the cellulose chains.

3.2.2. Encapsulation mechanism

3.2.2.1. Kinetic properties

3.2.2.1.1. Intra-particle diffusion behavior. The encapsulation reactions of OXPN into N.Ph and CF/N.Ph exhibit intra-particle diffusion curves of segmental properties and show three noticeable stages without intersections with the original points of the curves (Fig. 5A). This demonstrates the encapsulation of the OXPN by co-operated processes in addition to the significant effect of the diffusion mechanisms of the drug ions in the direction of the active receptors of N.Ph and CF/N.Ph.[40,41] This might involve (A) loading by active sight throughout the external surface (border), (B) intra-particle diffusion, and (C) the effect of the saturation or equilibrium stage.[42] The existence of the first stage signifies the operation of the external encapsulation processes during the initiation of the tests, and the efficiency of the encapsulation reactions during this stage is controlled by the quantities of the surficial active receptors (Fig. 5A).[43] By expanding the encapsulation duration, a new stage was detected, which signifies the operation of other mechanisms involving the effect of the OXPN diffusion processes and the layered encapsulation processes (Fig. 5A).[35,42] Finally, the third stage is detected as the dominant stage during the OXPN encapsulation equilibrium states of N.Ph and CF/N.Ph. This validates the occupation or consumption of the effective binding sites with the encapsulated OXPN molecules (Fig. 5A).[4,40] The encapsulation reactions during this stage are controlled by different mechanisms that might involve molecular interaction and/or the interionic attraction processes.[39]

3.2.2.1.2. Kinetic modeling. The kinetic properties of the OXPN encapsulation process into N.Ph (Fig. 5B) and CF/N.Ph (Fig. 5C) were illustrated based on the kinetic assumptions of both the pseudo-first order model (P.F) (eqn (4)) and the pseudo-second order (P.S) (eqn (5)) model. The agreement between the encapsulation processes and the kinetic models was assessed based on the non-linear fitting with their

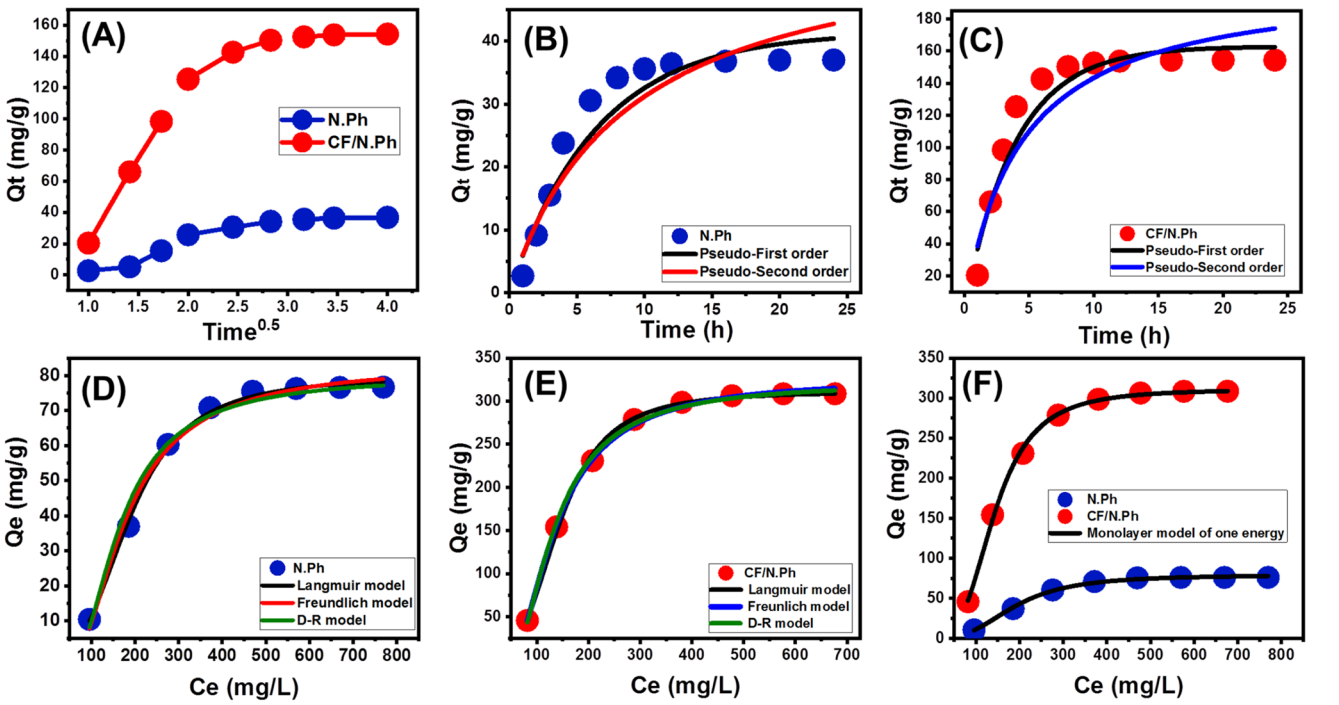

Fig. 5 Fitting of the OXPN encapsulation processes by N.Ph and CF/N.Ph with the different kinetic and isotherm models, including intra-particle diffusion model (A), pseudo-first order and pseudo-second order kinetic models (B) and (C), Langmuir, Freundlich, and D–R classic isotherm models (D) and (E), and monolayer advanced isotherm energy with one energy site (F).

equations considering both the correlation coefficient (R^2) and Chi-squared (χ^2) as the essential indicators of the fitting degree (Table 1 and Fig. 5B (N.Ph), and C (CF/N.Ph)).

$$Q_t = Q_e(1 - e^{-k_1 \cdot t}), \quad (4)$$

$$Q_t = \frac{Q_e^2 k_2 t}{1 + Q_e k_2 t}. \quad (5)$$

The detected values of R^2 and χ^2 indicate higher fitting of the OXPN encapsulation processes into N.Ph and CF/N.Ph with the

Table 1 The fitting parameters of the evaluated kinetic models, classic isotherm, advanced isotherm, Van't Hof formula, and release kinetic models

Model	Parameters	N.Ph	CF/N.Ph
Kinetic models			
Pseudo-first-order	K_1 (min^{-1})	0.154	0.254
	$Q_{e(Cal)}$ (mg g^{-1})	41.4	162.8
	R^2	0.94	0.95
	X^2	0.85	2.33
Pseudo-second-order	k_2 (g mg^{-1} min^{-1})	0.002	0.0011
	$Q_{e(Cal)}$ (mg g^{-1})	58.1	205.4
	R^2	0.92	0.91
	X^2	0.94	3.8
Isotherm models			
Langmuir	Q_{max} (mg g^{-1})	79.6	311.15
	b (L mg^{-1})	3.2×10^{-7}	1.99×10^{-7}
	R^2	0.98	0.98
	X^2	0.86	0.10
	R_L	0.99	0.99
Freundlich	$1/n$	0.49	0.69
	k_F (mg g^{-1})	83.07	325.34
	R^2	0.97	0.99
	X^2	1.76	0.087
D–R model	β (mol^2 kJ^{-2})	0.0085	0.01288
	Q_m (mg g^{-1})	79.9	321.85
	R^2	0.98	0.99
	X^2	0.29	0.102
	E (kJ mol^{-1})	7.65	6.23
Monolayer model of one energy	n	2.85	3.11
	N_M (mg g^{-1})	27.94	100.01
	$Q_{(sat)}$ (mg g^{-1})	79.6	311.03
	ΔE (kJ mol^{-1})	−8.42	−7.85
Thermodynamics			
ΔG^0 (kJ mol^{-1})	293.13	−10.64	−18.20
	303.13	−10.73	−18.96
	313.13	−10.76	−19.73
	323.13	−10.86	−20.52
ΔH^0 (kJ mol^{-1})		−8.7	−4.45
ΔS^0 (J K^{-1} mol^{-1})		6.61	11.68

Release kinetics

	Determination coefficient			
	Phillipsite		β-CD/Ph	
Models	Acetate buffer (pH 5.5)	Phosphate buffer (pH 7.4)	Acetate buffer (pH 5.5)	Phosphate buffer (pH 7.4)
Zero-order	0.89	0.89	0.86	0.94
First order	0.98	0.97	0.93	0.98
Higuchi	0.99	0.98	0.97	0.99
Hixson–Crowell	0.95	0.96	0.98	0.97
Korsmeyer–peppas	0.99	0.96	0.98	0.98
n	0.87	0.53	0.53	0.57

kinetic properties of the P.F model than the evaluated P.S model. These fitting results were also confirmed based on the notable agreement between the previously detected experimental equilibrium capacities ($Q_{e(exp)} = 37$ mg g^{-1} (N.Ph) and 154.3 mg g^{-1} (CF/N.Ph)) and theoretically obtained values as a mathematical parameter of the P.F model ($Q_{e(theo)} = 41.4$ mg g^{-1} (N.Ph) and 162.8 mg g^{-1} (CF/N.Ph)) (Table 1). According to the kinetic properties of the P.F model, the encapsulation of OXPN into N.Ph and CF/N.Ph occurred mainly by physical mechanisms that might involve strong effects of van der Waals forces and electrostatic attractions.[44,45] However, the OXPN encapsulation processes highly fitted with the P.F model compared to the P.S model, and the occurred processes still show considerable agreement with the kinetic behavior of the P.S model. Therefore, it was expected that there would be a minor impact or assistant effect for some weak chemical processes during the OXPN encapsulation processes into N.Ph and CF/N.Ph, such as hydrogen bonding, hydrophobic interactions, electron sharing, and chemical complexes.[40,44] The cooperation of both physical and chemical mechanisms involves the formation of a chemically encapsulated layer of the drug, followed by the formation of a physically encapsulated layer using the first layer as the substrate.[46]

3.2.2.2. Equilibrium properties

3.2.2.2.1. Classic isotherm models. The equilibrium properties of the OXPN encapsulation processes into N.Ph and CF/N.Ph were illustrated based on the isotherm assumptions of the Langmuir model (eqn (6)), Freundlich model (eqn (7)), and Dubinin–Radushkevich (D–R) model (eqn (8)). The agreement between the encapsulation processes and the isotherm models were assessed based on the non-linear fitting with their equations considering both the correlation coefficient (R^2) and Chi-squared (χ^2) as the essential indicators of the fitting degree (Table 1 and Fig. 5D (N.Ph), and E (CF/N.Ph)).

$$Q_e = \frac{Q_{max} b C_e}{(1 + bC_e)} \quad (6)$$

$$Q_e = K_f C_e^{1/n} \quad (7)$$

$$Q_e = Q_m e^{-\beta \varepsilon_2} \quad (8)$$

The detected values of R^2 and χ^2 indicate higher fitting of the OXPN encapsulation processes into N.Ph with the equilibrium properties of the Langmuir model than the Freundlich model. This agreement with the Langmuir isotherm suggests the encapsulation of OXPN homogeneously into the N.Ph particles and in monolayer form.[44,45] Moreover, the estimated RL parameter of the OXPN encapsulation reaction exhibits a value less than unity, which is normally an indicator of the favorable properties of the reactions that occur.[4,43] Regarding the synthetic CF/N.Ph composite, the functionalization of phillipsite with cellulose resulted in a considerable impact on its equilibrium properties as a potential carrier of OXPN. The OXPN encapsulation processes into CF/N.Ph exhibit slightly higher agreement with the isotherm assumption of the Freundlich equation than the Langmuir equation. Therefore, the encapsulation reaction might occur heterogeneously in multilayer forms.[35] As an estimated parameter from the Langmuir isotherm study, the expected maximum OXPN encapsulation capacities ($Q_{e\ max}$) of N.Ph and CF/N.Ph are 79.6 mg g^{-1} and 311.15 mg g^{-1}, respectively.

The D–R model as an equilibrium model is highly effective in elucidating the energetic heterogeneity of N.Ph and CF/N.Ph during the OXPN encapsulation processes regardless of the types of the surface either homogenous or heterogeneous.[47] The Gaussian energy (E) obtained as a mathematical parameter of the D–R model indicates the nature of the OXPN encapsulation mechanisms (chemical or physical). Encapsulation processes, which display E value <8 kJ mol^{-1}, from 8 to 16 kJ mol^{-1} and >16 kJ mol^{-1}, suggest the operation of strong physical, weak chemical or complex physical/chemical, and strong chemical encapsulation mechanisms.[4,47] The values of the E parameter estimated for N.Ph (7.65 kJ mol^{-1}) and CF/N.Ph (6.23 kJ mol^{-1}) are within the reported range of physical mechanisms but also within the signified range of zeolitic ion exchange mechanisms (0.6–25 kJ mol^{-1}), matching the theoretical findings of the kinetic studies (Table 1).

3.2.2.2.2. Advanced isotherm models. The assumptions of the advanced isotherm models according to the mathematical and physical basics of statistical physics theory strongly signify the encapsulation mechanism in terms of the surficial properties of N.Ph and CF/N.Ph in addition to their interactive interface with the OXPN molecules. Here, a monolayer isotherm model with one energy site (eqn (9)) was applied to describe the equilibrium properties of N.Ph and CF/N.Ph as potential carriers of OXPN based on its related steric and energetic parameters (Fig. 5F and Table 1).

$$Q = nN_o = \frac{nN_M}{1 + \left(\frac{C_{1/2}}{C_e}\right)^n} = \frac{Q_o}{1 + \left(\frac{C_{1/2}}{C_e}\right)^n} \quad (9)$$

The steric parameters (active OXPN encapsulation sites density of N.Ph and CF/N.Ph ($N_{M(OXPN)}$), number of encapsulated OXPN per one active site ($n_{(OXPN)}$), and encapsulation capacities of OXPN at the saturation states of N.Ph and CF/N.Ph ($Q_{sat(OXPN)}$)) and energetic parameter (OXPN encapsulation energy) are presented in Table 1. Based on the steric parameters, the functionalization of phillipsite with cellulose resulted in a notable enhancement in the qualification of the CF/N.Ph composite as a potential carrier of OXPN compared to raw N.Ph. The quantities of the effective free active site during the OXPN encapsulation increased strongly after the integration of cellulose ($N_{M(OXPN)} = 27.94$ mg g^{-1} (N.Ph) and 100 mg g^{-1} (CF/N.Ph)), which might be related to the integrated new active functional groups of cellulose or the increase in the interaction interface with the notable increase in the surface area (Table 1). The significant increase in the values of $N_{M\ (OXPN)}$ of CF/N.Ph strongly induced its loading capacity at the saturation states of its incorporated particles to be 311 mg g^{-1} compared to 79.65 mg g^{-1} for N.Ph. The detected numbers of the encapsulated OXPN ion in each free site of N.Ph and CF/N.Ph ($n_{(OXPN)} =$

2.85 (N.Ph) and 3.11 (CF/N.Ph)) is >1, suggesting the vertical orientation of the loaded ions and their encapsulation by multi-molecular mechanisms (Table 1).[48,49] Moreover, these n (OXPN) values validate the efficiency of CF/N.Ph to capture about 4 OXPN molecules per site, which is higher than N.Ph, in which each site can be loaded with 3 OXPN molecules.

The energies of the OXPN encapsulation processes (ΔE) into N.Ph and CF/N.Ph were determined based on eqn (10) by considering OXPN rest concentration at the half saturations of N.Ph and CF/N.Ph ($C_{1/2}$) as well as the absolute solubility of OXPN (Table 1):

$$\Delta E = -RT \ln\left(\frac{S}{C_{\frac{1}{2}}}\right). \quad (10)$$

The estimated values of ΔE during the OXPN processes using N.Ph and CF/N.Ph are 8.42 kJ mol^{-1} and 7.85 kJ mol^{-1}, respectively. These energetic values significantly match the previously reported suggestion based on kinetic and classic isotherm studies about the essential mechanistic impact of physical processes and weak chemical reactions, as the ΔE values are ≤40 kJ mol^{-1}.[48] The effective mechanistic processes might involve van der Waals forces (ΔE = 4 to 10 kJ mol^{-1}), dipole bonding forces (ΔE = 2 to 29 kJ mol^{-1}), and hydrogen bonding (ΔE < 30 kJ mol^{-1}).[26,50]

3.2.2.3. Thermodynamic properties. The thermodynamic properties of the OXPN encapsulation reactions by N.Ph and CF/N.Ph were evaluated by considering the temperature range from 20 °C to 50 °C at adjusted values of the other affecting variables [duration: 24 h; dosage: 20 mg; concentration: 800 mg L^{-1}; pH: 9; and volume: 50 mL]. The thermodynamic properties involved essential functions, such as Gibbs free energy (ΔG^0) (eqn (12)), in addition to the entropy (ΔS^0) and enthalpy (ΔH^0) of the reactions, which were determined as parameters from the linear regression fitting using Van't Hof equation (eqn (12)) (Fig. 6):[51]

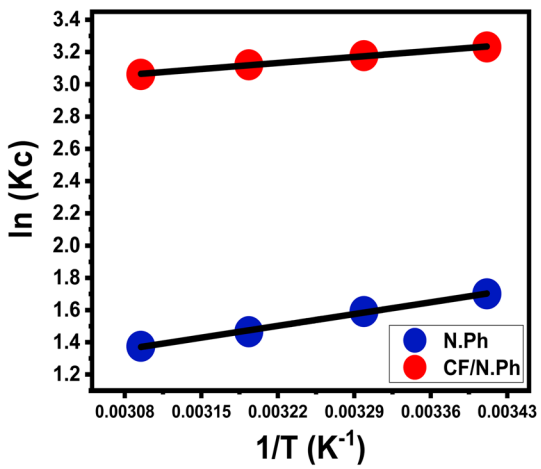

Fig. 6 Fitting of the OXPN encapsulation results with Van't Hof thermodynamic equation.

$$\ln(K_c) = \frac{\Delta S^0}{R} - \frac{\Delta H^0}{RT}, \quad (11)$$

$$\Delta G^0 = -RT \ln K_c \quad (12)$$

The detection of ΔG^0 and ΔH^0 with negatively signed values reveals the spontaneous, exothermic, and favorable behaviors of the OXPN encapsulation reactions either by N.Ph or CF/N.Ph (Table 1). Moreover, the positively signed ΔS^0 values obtained using both N.Ph and CF/N.Ph resulted in an increase in the randomness of the occurred OXPN encapsulation reactions in terms of the tested temperature.

3.3. *In vitro* release profiles

The OXPN release properties from the structures of N.Ph and CF/N.Ph was assessed based on the determined diffused percentages of the drug molecules within the two buffers (phosphate (pH 7.4) and acetate (pH 5.5)) used to simulate the environment and conditions of the tumor cells (Fig. 7). The measured OXPN diffused percentages from both N.Ph and CF/N.Ph with the two studied buffers demonstrated observable changes in the recognized rates with a significant increase in the assessed release duration (Fig. 7A and B). The OXPN release rates from N.Ph and CF/N.Ph exhibit fast properties that are associated with remarkable changes in the released quantities of OXPN. After certain release intervals, the actual OXPN diffusion rates weakened notably, and no considerable increase in released qualities could be detected and finally appeared to be fixed at the end of the tests. The rapid OXPN diffusion rates during the beginning release intervals were attributed to the fast desorption of the molecules of the drug immediately from the adsorption sites of N.Ph and CF/N.Ph.[52,53] After the complete desorption of the weakly bonded and surficial loaded OXPN molecules, the release properties became controlled by the diffusion of the strongly bonded molecules in chemically complexed forms, in addition to the trapped OXPN ions within the structural pores of the phillipsite, which adversely affected the determined diffusion rates.[7,51] Furthermore, the observed OXPN release profiles of N.Ph and CF/N.Ph reflected a significant accelerating impact of the acidic conditions (pH 5.5 (acetate buffer)) on the release process compared to the basic conditions (pH 7.4 (phosphate buffer)). The faster OXPN release properties at pH 5.5 than at pH 7.4 was attributed to the notable enhancement in the drug's mobility, solubility, and diffusion properties with the decrease in the pH.[15]

The experimental OXPN release profiles of N.Ph either at the phosphate buffer or the acetate buffer extended to about 180 h without any experimental detection of the complete release states (100% release percentage) (Fig. 7A and B). About 50% of the encapsulated quantity of OXPN was diffused from the structure of N.Ph after 60 h and 45 h at pH 5.5 and pH 7.4, respectively. The maximum OXPN release percentages in the phosphate buffer and the acetate buffer after 180 h are 76.8% and 82%, respectively. Regarding the profiles of CF/N.Ph, it shows notably faster release properties than N.Ph (Fig. 7A and B).

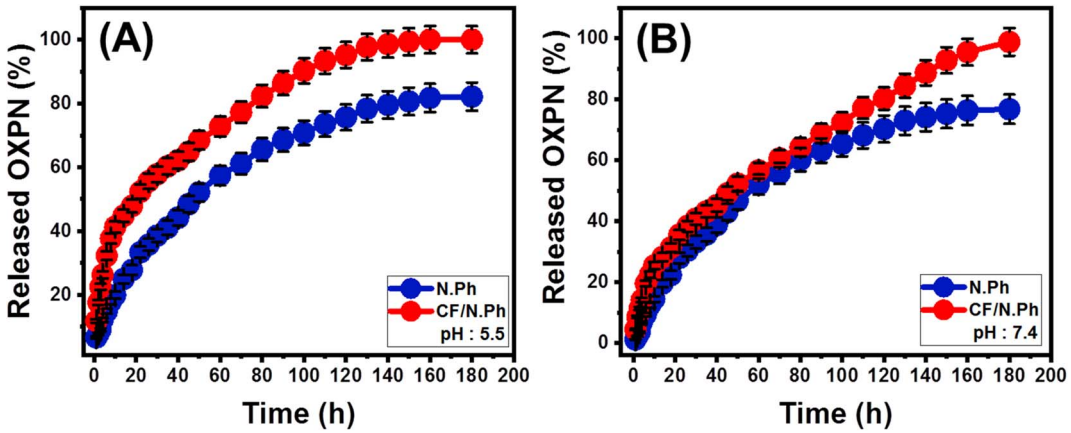

Fig. 7 The OXPN release profiles of N.Ph (A) and C/N.Ph (B) at acetate buffer (pH 5.5) and phosphate buffer (pH 7.4).

About 50% of the encapsulated quantity of OXPN was diffused from the structure of CF/N.Ph after 45 h and 22 h at pH 5.5 and pH 7.4, respectively. However, complete diffusion in the acetate buffer was detected after about 150 h, and the maximum diffusion in the phosphate buffer after 180 h was 98%. The higher OXPN release properties of CF/N.Ph than N.Ph strongly signify the remarkable impact of the integrated cellulose structure on the properties of phillipsite as a natural zeolite (Fig. 7A and B). The common formation of chemical complexes between the active functional groups of OXPN and the reactive chemical structure of the zeolite, in addition to the expected trapping of the drug ions within the structural nanopores of phillipsite, exhibits a strong adverse effect on the efficiency of the diffusion or desorption reactions of the encapsulated ions.[17,54] Therefore, the functionalization process of phillipsite with cellulose provides considerable barriers between the drug and the reactive groups of zeolite, reducing the quantities of the formed complexes and the quantities of trapped ions.[17,52,54] Moreover, the integrated cellulose fibers provided additional free sites for surficial loading processes that prompted the release properties. The slow and controlled delivery of OXPN as anticancer chemotherapy is recommended in specific cases that require long-term interaction and exposure between the drug ions and the tumor cells.[6,7] Additionally, very fast and abrupt delivery processes are recommended in some cases that require certain therapeutic dosages within short intervals. Therefore, the synthetic CF/N.Ph as a potential carrier of OXPN can provide a favorable delivery system that exhibits controlled encapsulation and release properties.

3.4. Release kinetic studies

The kinetic studies of the OXPN release processes from N.Ph and CF/N.Ph were performed as an indication of the controlled mechanistic processes. Modeling of the release reactions according to zero-order (Z-O) (eqn (13)), first-order (F-O) (eqn (14)), Higuchi (H–G) (eqn (15)), Hixson–Crowell (H–C) (eqn (16)), and Korsmeyer–Peppas (K–P) (eqn (17)) release kinetic models was used to illustrate the mechanisms based on the linear regression fitting degrees with these models:[7]

$$W_t - W_0 = K_0 \cdot t, \tag{13}$$

$$\ln(W_\infty / W_t) = K_1 \cdot t, \tag{14}$$

$$W_t = K_h t^{1/2}, \tag{15}$$

$$W_0^{1/3} - W_t^{1/3} = K_{HC} t, \tag{16}$$

$$W_t / W_\infty = K_p t^n. \tag{17}$$

The zero-order kinetics properties validate the occurrence of the release reactions at constant rates without considerable impacts of the dosages of the loaded OXPN drug on the release efficiencies of N.Ph and CF/N.Ph.[17] Regarding the F–O release kinetics, the OXPN encapsulated dosages into N.Ph and CF/N.Ph strongly affect the release efficiencies.[1] The mechanistic assumption of Higuchi kinetics (H–G) donates the dominant impact of the diffusion mechanisms during the release processes.[1,55] The diffusion mechanisms based on Higuchi kinetics occurred at a fixed rate lower than the encapsulated OXPN quantities. Moreover, the used carriers must exhibit sink properties, and their swelling and solubility display a neglected impact on the release behaviors.[17] The mechanistic assumption of the Hixson–Crowell model (H–C) involves erosion reactions rather than diffusion with significant influence on the surface area and diameter of the tested particles of the carriers.[17,56] Regarding the mechanistic assumption of Korsmeyer–Peppas kinetics, the release processes involve the cooperation of diffusion and erosion reactions.[1,57]

Based on the determination coefficients (R^2), the occurred OXPN release reactions of N.Ph and CF/N.Ph follow the properties of the F–O (Fig. 8C, D and Table 1) model rather than the Z–O model (Fig. 8A, B and Table 1), reflecting the strong influence of the encapsulated OXPN dosages on the release performances. The release reactions show excellent agreement with both Higuchi (H–G) (Fig. 8E, F and Table 1) and Hixson–Crowell (H–C) models (Fig. 8G, H and Table 1). These kinetic assessment results suggest the cooperation of diffusion and erosion processes during the OXPN release reactions. This mechanistic suggestion was supported by the recognized significant fitting

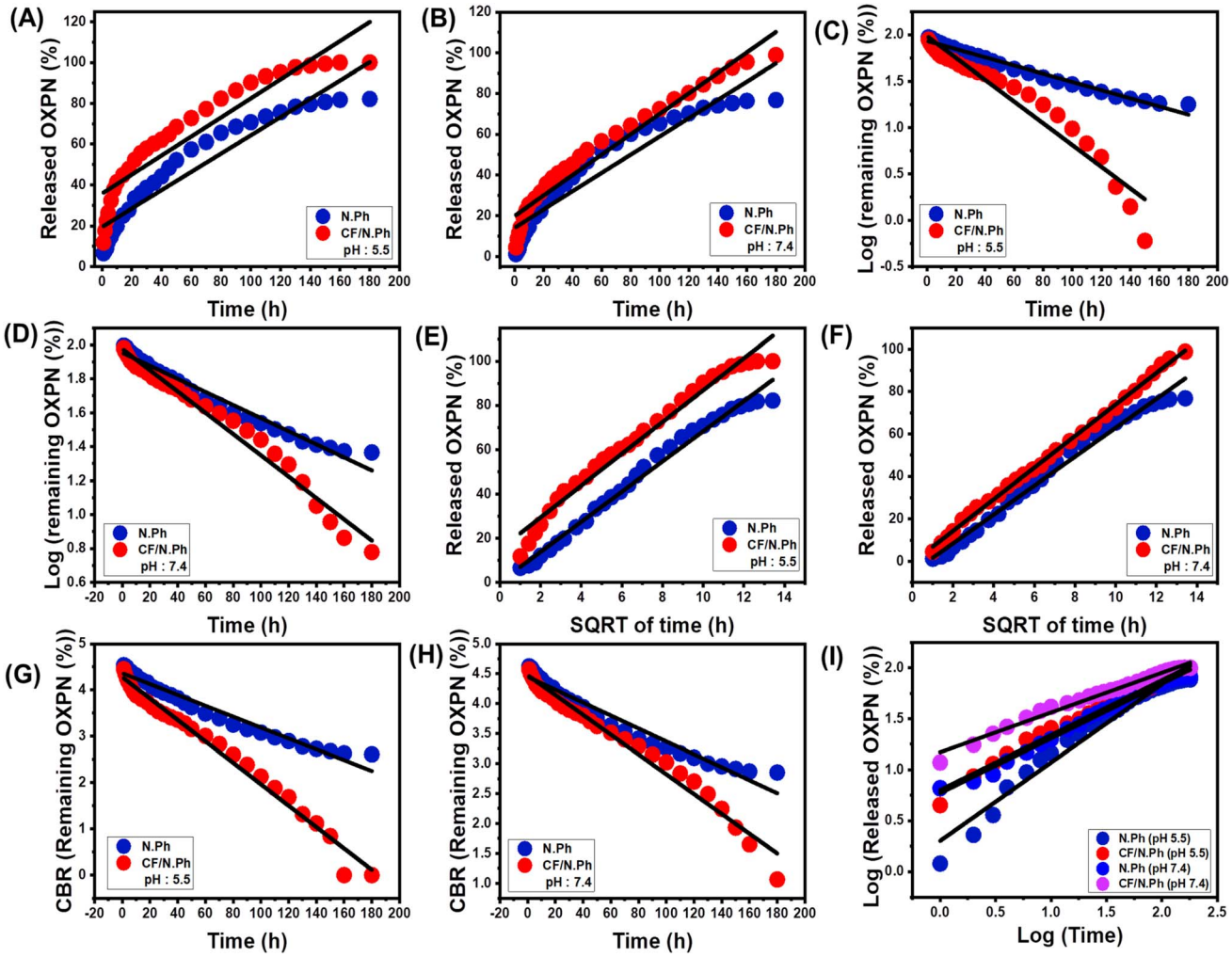

Fig. 8 Fitting of the OXPN release results with the zero-order model (A) and (B), first-order model (C) and (D), Higuchi model (E) and (F), Hixson–Crowell model (G) and (H), and Korsmeyer–Peppas model (I).

degrees of the Korsmeyer–Peppas and the estimated values of diffusion exponent (n) as a fitting parameter (Fig. 8I and Table 1). The values of the diffusion exponent (n) are higher than 0.45, validating the non-Fickian transport properties of the release reactions of the N.Ph and CF/N.Ph delivery systems.[37]

3.5. Cytotoxicity properties

The cytotoxic effect of the free CF/N.Ph particles on normal colorectal fibroblast cells (CCD-18Co) was evaluated as an essential factor for assessing the biocompatibility and safety value of the studied cancer on normal and non-infected cells. The cytotoxicity of free CF/N.Ph particles, as well as their OXPN-loaded products, was evaluated against the target human colorectal cancer cell (HCT-116) to determine its value as an anticancer agent and as a carrier of enhanced impact on the therapeutic effect of the loaded OXPN drug. Regarding the cytotoxic effect of free CF/N.Ph particles on the CCD-18Co normal cells, the composite particles displayed high biocompatible and safe properties on the normal cell lines within the evaluated experimental range of the applied dosages (20 to 120 μg L^{-1}). The measured cell viability percentage during the treatment of the CCD-18Co normal cells with the highest tested dosage of the free CF/N.Ph particles (120 μg L^{-1}) is 81.7%. Regarding the cytotoxic impacts of the free CF/N.Ph particles on the infected HCT-116 cells, the synthetic composite as free particles displayed considerable cytotoxicity against the tumor cells, especially at the applied dosages higher than 50 μg mL^{-1} (Fig. 9A). The measured cell viability percentage, inhibitory percentage, and IC-50 value in the presence of 500 μg mL^{-1} of free CF/N.Ph particles are 46.91%, 53.09%, and 176.4 μg mL^{-1}, respectively (Fig. 9A). Such cytotoxic results validate the promising biological activity of CF/N.Ph and its considerable oxidation impact on colorectal cancer cells. Regarding the cytotoxicity properties of OXPN encapsulated on HCT-116 cancer cells, the application of the same dosage of the free particles (500 μg mL^{-1}) resulted in a 3.14% cell viability percentage, 96.86% inhibitory percentage, and 57.23 μg mL^{-1} as IC-50 (Fig. 9B). Such cytotoxic results demonstrate the remarkable enhancement impact of the used CF/N.Ph carrier

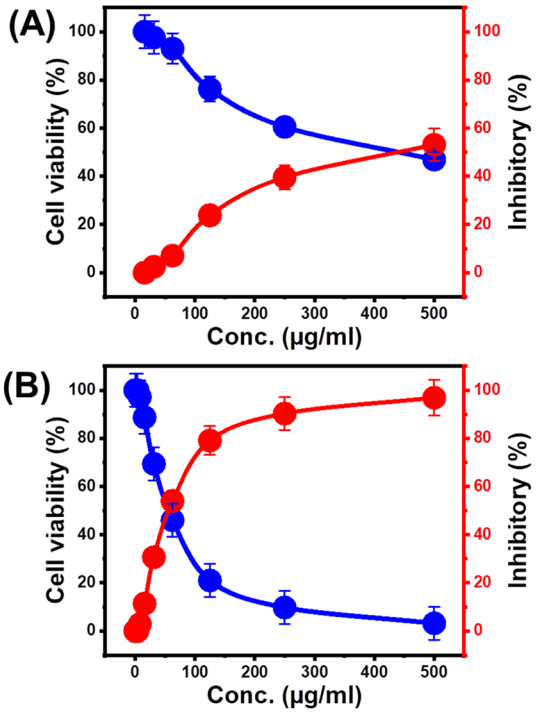

Fig. 9 The cytotoxicity effect of free CF/N.Ph (A) and OXPN encapsulated CF/N.Ph (B) on colorectal cancer cell (HCT-116).

on the cytotoxic effects, and the therapeutic impact of the loaded OXPN drug as common chemotherapy in addition to its previously determined controlling effects on the loading and release behaviors.

4 Conclusion

Phillipsite was hybridized with cellulose to form an innovative structure (CF/N.Ph), which was characterized as a potential multifunctional carrier of oxaliplatin (OXPN) chemotherapy. CF/N.Ph exhibited enhanced OXPN encapsulation properties (311.03 mg g^{-1}) than N.Ph (79.6 mg g^{-1}). This was attributed to the enhancement in organic affinity, surface area, and active site density (100.01 mg g^{-1} (CF/N.Ph) and 27.94 mg g^{-1} (N.Ph)). The loading process into CF/N.Ph involved the encapsulation of 4 OXPN molecules per site. The encapsulation process was controlled by physical mechanisms, such as electrostatic attraction and van der Waals forces, according to the energy of the reaction (<40 kJ mol^{-1}). The release profile of CF/N.Ph shows slow and controlled properties for more than 150 h. This occurred according to complex erosion/diffusion mechanisms based on the release kinetics and diffusion exponent (>0.45). The cell viability of HCT-116 cancer cells after treatment with free CF/N.Ph (46.91%) and OXPN-loaded product (3.14%) demonstrates strong inhibition effects on the cancer cells.

Conflicts of interest

There are no conflicts to declare.

Acknowledgements

This work was funded by the Deanship of Scientific Research at Princess Nourah bint Abdulrahman University, through the Research Groups Program Grant no. (RGP-1443-0042).

References

1 H. M. El-Zeiny, M. R. Abukhadra, O. M. Sayed, A. H. Osman and S. A. Ahmed, Insight into novel β-cyclodextrin-grafted poly (Nvinylcaprolactam) nanogel structures as advanced carriers for 5- fluorouracil: Equilibrium behavior and pharmacokinetic modeling, *Colloids Surf., A*, 2020, **586**, 124197.

2 E. S. Cutrim, A. A. Vale, D. Manzani, H. S. Barud, E. R. Castellon, A. P. Santos and A. C. Alcântara, Preparation, characterization and in vitro anticancer performance of nanoconjugate based on carbon quantum dots and 5-Fluorouracil, *Mater. Sci. Eng., C*, 2021, **120**, 111781.

3 S. M. Abuzar, E. J. Park, Y. Seo, J. Lee, S. H. Baik and S. J. Hwang, Preparation and evaluation of intraperitoneal long-acting oxaliplatin-loaded multi-vesicular liposomal depot for colorectal cancer treatment, *Pharmaceutics*, 2020, **12**(8), 736.

4 M. A. Sayed, H. M. El-Zeiny, J. S. Khim, J. S. Ajarem, A. A. Allam and M. R. Abukhadra, Insight into the loading properties of Na+ green functionalized clinoptilolite as a potential carrier for the 5-fluorouracil drug, its release kinetics, and cytotoxicity, *ACS Omega*, 2022, **7**(8), 6991–7001.

5 Y. Ren, X. Li, B. Han, N. Zhao, M. Mu, C. Wang, Y. Du, Y. Wang, A. Tong, Y. Liu and L. Zhou, Improved anti-colorectal carcinomatosis effect of tannic acid co-loaded with oxaliplatin in nanoparticles encapsulated in thermosensitive hydrogel, *Eur. J. Pharm. Sci.*, 2019, **128**, 279–289.

6 P. Sundaramoorthy, T. Ramasamy, S. K. Mishra, K. Y. Jeong, C. S. Yong, J. O. Kim and H. M. Kim, Engineering of caveolae-specific self-micellizing anticancer lipid nanoparticles to enhance the chemotherapeutic efficacy of oxaliplatin in colorectal cancer cells, *Acta Biomater.*, 2016, **42**, 220–231.

7 L. Tian, M. R. Abukhadra, A. S. Mohamed, A. Nadeem, S. F. Ahmad and K. E. Ibrahim, Insight into the loading and release properties of an exfoliated kaolinite/cellulose fiber (EXK/CF) composite as a carrier for oxaliplatin drug: cytotoxicity and release kinetics, *ACS Omega*, 2020, **5**(30), 19165–19173.

8 R. A. Praphakar, M. Jeyaraj, S. Mehnath, A. Higuchi, D. Ponnamma, K. K. Sadasivuni and M. Rajan, A pH-sensitive guar gum-grafted-lysine-β-cyclodextrin drug carrier for the controlled release of 5-flourouracil into cancer cells, *J. Mater. Chem.*, 2018, **6**, 1519–1530.

9 J. E. Lee, S. M. Abuzar, Y. Seo, H. Han, Y. Jeon, E. J. Park, S. H. Baik and S. J. Hwang, Oxaliplatin-loaded chemically cross-linked hydrogels for prevention of postoperative abdominal adhesion and colorectal cancer therapy, *Int. J. Pharm.*, 2019, **565**, 50–58.

10 A. M. Itoo, M. Paul, B. Ghosh and S. Biswas, Oxaliplatin delivery via chitosan/vitamin E conjugate micelles for improved efficacy and MDR-reversal in breast cancer, *Carbohydr. Polym.*, 2022, **282**, 119108.
11 Y. Li, Z. Sun, Y. Cui, H. Zhang, S. Zhang, X. Wang, S. Liu and Q. Gao, Oxaliplatin derived monofunctional triazole-containing platinum (II) complex counteracts oxaliplatin-induced drug resistance in colorectal cancer, *Bioorg. Chem.*, 2021, **107**, 104636.
12 N. Altoom, S. M. Ibrahim, S. I. Othman, A. A. Allam, H. A. Alqhtani, F. S. Al-Otaibi and M. R. Abukhadra, Characterization of β-cyclodextrin/phillipsite (β-CD/Ph) composite as a potential carrier for oxaliplatin as therapy for colorectal cancer; loading, release, and cytotoxicity, *Colloids Surf., A*, 2022, **648**, 129144.
13 P. M. Shad, S. Z. Karizi, R. S. Javan, A. Mirzaie, H. Noorbazargan, I. Akbarzadeh and H. Rezaie, Folate conjugated hyaluronic acid coated alginate nanogels encapsulated oxaliplatin enhance antitumor and apoptosis efficacy on colorectal cancer cells (HT29 cell line), *Toxicol. In Vitro*, 2020, **65**, 104756.
14 N. Rabiee, M. Atarod, M. Tavakolizadeh, S. Asgari, M. Rezaei, O. Akhavan, A. Pourjavadi, M. Jouyandeh, E. C. Lima, A. H. Mashhadzadeh and A. Ehsani, Green metal-organic frameworks (MOFs) for biomedical applications, *Microporous Mesoporous Mater.*, 2022, **335**, 111670.
15 A. Narmani, M. Kamali, B. Amini, A. Salimi and Y. Panahi, Targeting delivery of oxaliplatin with smart PEG-modified PAMAM G4 to colorectal cell line: In vitro studies, *Process Biochem.*, 2018, **69**, 178–187.
16 S. P. Bandi and V. V. K. Venuganti, Functionalized polymeric patch for localized oxaliplatin delivery to treat gastric cancer, *Mater. Sci. Eng., C*, 2021, **128**, 112302.
17 S. I. Othman, A. A. Allam, H. AlFassam, G. M. Abu-Taweel, N. Altoom and M. R. Abukhadra, Sonoco green decoration of clinoptilolite with MgO nanoparticles as a potential carrier for 5-fluorouracil drug: loading behavior, release profile, and cytotoxicity, *J. Inorg. Organomet. Polym.*, 2021, **31**, 4608–4622.
18 M. Servatan, P. Zarrintaj, G. Mahmodi, S. J. Kim, M. R. Ganjali, M. R. Saeb and M. Mozafari, Zeolites in drug delivery: Progress, challenges and opportunities, *Drug Discovery Today*, 2020, **25**, 642–656.
19 M. Sandomierski, Z. Buchwald, W. Koczorowski and A. Voelkel, Calcium forms of zeolites A and X as fillers in dental restorative materials with remineralizing potential, *Microporous Mesoporous Mater.*, 2020, **294**, 109899.
20 I. M. Souza, C. I. Sainz-Díaz, C. Viseras and S. B. Pergher, Adsorption capacity evaluation of zeolites as carrier of isoniazid, *Microporous Mesoporous Mater.*, 2020, **292**, 109733.
21 C. Serri, B. de Gennaro, L. Catalanotti, P. Cappelletti, A. Langella, M. Mercurio, L. Mayol and M. Biondi, Surfactant-modified phillipsite and chabazite as novel excipients for pharmaceutical applications, *Microporous Mesoporous Mater.*, 2016, **224**, 143–148.
22 M. Markovic, A. Dakovic, G. E. Rottinghaus, M. Kragovic, A. Petkovic, D. Krajisnik, J. Milic, M. Mercurio and B. de Gennaro, Adsorption of the mycotoxin zearalenone by clinoptilolite and phillipsite zeolites treated with cetylpyridinium surfactant, *Colloids Surf., B*, 2017, **151**, 324–332.
23 M. R. Abukhadra and A. S. Mohamed, Adsorption removal of safranin dye contaminants from water using various types of natural zeolite, *Silicon*, 2019, **11**(3), 1635–1647.
24 L. Bandura, M. Białoszewska, S. Malinowski and W. Franus, Adsorptive performance of fly ash-derived zeolite modified by β-cyclodextrin for ibuprofen, bisphenol A and caffeine removal from aqueous solutions–equilibrium and kinetic study, *Appl. Surf. Sci.*, 2021, **562**, 150160.
25 S. Lu, Q. Liu, R. Han, J. Shi, M. Guo, C. Song, N. Ji, X. Lu and D. Ma, Core-shell structured Y zeolite/hydrophobic organic polymer with improved toluene adsorption capacity under dry and wet conditions, *Chem. Eng. J.*, 2021, **409**, 128194.
26 M. T. Ashraf, A. A. AlHammadi, A. M. El-Sherbeeny, S. Alhammadi, W. Al Zoubi, Y. G. K. Supervison and M. R. Abukhadra, Synthesis of cellulose fibers/Zeolite-A nanocomposite as an environmental adsorbent for organic and inorganic selenium ions; characterization and advanced equilibrium studies, *J. Mol. Liq.*, 2022, **360**, 119573.
27 B. F. Dizaji, M. H. Azerbaijan, N. Sheisi, P. Goleij, T. Mirmajidi, F. Chogan, M. Irani and F. Sharafian, Synthesis of PLGA/chitosan/zeolites and PLGA/chitosan/metal organic frameworks nanofibers for targeted delivery of Paclitaxel toward prostate cancer cells death, *Int. J. Biol. Macromol.*, 2020, **164**, 1461–1474.
28 M. Pooresmaeil, S. Javanbakht, S. B. Nia and H. Namazi, Carboxymethyl cellulose/mesoporous magnetic graphene oxide as a safe and sustained ibuprofen delivery bio-system: Synthesis, characterization, and study of drug release kinetic, *Colloids Surf., A*, 2020, **594**, 124662.
29 M. Rahaman, M. Rahman, S. M. Alam, M. Sultana, M. Parvez and A. Ahmed, Preparation and Characterization of Mustard Stalks Derived Carboxymethyl Cellulose and Poly (L-Lactic Acid) Biocomposites, *SSRN Electronic Journal*, 2021, DOI: **10.2139/ssrn.3899839**.
30 M. M. Treacy and J. B. Higgins, *Collection of Simulated XRD Powder Patterns for Zeolites Fifth*, 5th edn, Elsevier, 2007, revised edition.
31 M. Shaban and M. R. Abukhadra, Geochemical evaluation and environmental application of Yemeni natural zeolite as sorbent for Cd2+ from solution: kinetic modeling, equilibrium studies, and statistical optimization, *Environ. Earth Sci.*, 2017, **76**, 310.
32 Y. Chen, L. Zhang, C. Mei, Y. Li, G. Duan, S. Agarwal, A. Greiner, C. Ma and S. Jiang, Wood-inspired anisotropic cellulose nanofibril composite sponges for multifunctional applications, *ACS Appl. Mater. Interfaces*, 2020, **12**(31), 35513–35522.
33 K. Ullah, S. A. Khan, G. Murtaza, M. Sohail, A. Manan and A. Afzal, Gelatin-based hydrogels as potential biomaterials for colonic delivery of oxaliplatin, *Int. J. Pharm.*, 2019, **556**, 236–245.
34 C. Liang, H. Wang, M. Zhang, W. Cheng, Z. Li, J. Nie, G. Liu, D. Lian, Z. Xie, L. Huang and X. Zeng, Self-controlled release of oxaliplatin prodrug from d- α-tocopheryl polyethylene glycol 1000 succinate (TPGS) functionalized mesoporous

silica nanoparticles for cancer therapy, *J. Colloid Interface Sci.*, 2018, **525**, 1–10.

35 M. R. Abukhadra, F. A. El Kashief, S. I. Othman, H. A. Alqhtani and A. A. Allam, Synthesis and characterization of Fe0@ chitosan/cellulose biocompatible composites from natural resources as advanced carriers for ibuprofen drug: reaction kinetics and equilibrium, *New J. Chem.*, 2022, **46**(26), 12797–12807.

36 K. Lenz, S. Hann, G. Koellensperger, Z. Stefanka, G. Stingeder, N. Weissenbacher, S. N. Mahnik and M. Fuerhacker, Presence of cancerostatic platinum compounds in hospital wastewater and possible elimination by adsorption to activated sludge, *Sci. Total Environ.*, 2005, **345**(1–3), 141–152.

37 M. R. Abukhadra, N. M. Refay, A. M. El-Sherbeeny, A. M. Mostafa and M. A. Elmeligy, Facile synthesis of bentonite/biopolymer composites as low-cost carriers for 5-fluorouracil drug; equilibrium studies and pharmacokinetic behavior, *Int. J. Biol. Macromol.*, 2019, **141**, 721–731.

38 M. Salam, M. Mokhtar, S. M. Albukhari, D. F. Baamer, L. Palmisano, M. Jaremko and M. R. Abukhadra, Synthesis and Characterization of Green ZnO@ polynaniline/ Bentonite Tripartite Structure (G. Zn@ PN/BE) as Adsorbent for As (V) Ions: Integration, Steric, and Energetic Properties, *Polymers*, 2022, **14**(12), 2329.

39 Y. Jiang, M. R. Abukhadra, N. M. Refay, M. F. Sharaf, M. A. El-Meligy and E. M. Awwad, Synthesis of chitosan/MCM-48 and β-cyclodextrin/MCM-48 composites as bio-adsorbents for environmental removal of Cd2+ ions; kinetic and equilibrium studies, *React. Funct. Polym.*, 2020, **154**, 104675.

40 M. A. Salam, M. R. Abukhadra and M. Mostafa, Effective decontamination of As (V), Hg (II), and U (VI) toxic ions from water using novel muscovite/zeolite aluminosilicate composite: adsorption behavior and mechanism, *Environ. Sci. Pollut. Res.*, 2020, **27**(12), 13247–13260.

41 E. El Qada, Kinetic Behavior of the Adsorption of Malachite Green Using Jordanian Diatomite as Adsorbent, *Jordanian J. Eng. Chem. Ind.*, 2020, **3**(1), 1–10.

42 X. Lin, Y. Xie, H. Lu, Y. Xin, R. Altaf, S. Zhu and D. Liu, Facile preparation of dual La-Zr modified magnetite adsorbents for efficient and selective phosphorus recovery, *Chem. Eng. J.*, 2021, **413**, 127530.

43 S. M. Albukhari, M. A. Salam and M. R. Abukhadra, Effective retention of inorganic Selenium ions (Se (VI) and Se (IV)) using novel sodalite structures from muscovite; characterization and mechanism, *J. Taiwan Inst. Chem. Eng.*, 2021, **120**, 116–126.

44 A. Sherlala, M. M. Raman and A. Bello, Buthiyappan, Adsorption of arsenic using chitosan magnetic graphene oxide nanocomposite, *J. Environ. Manage.*, 2019, **246**, 547–556.

45 Y. Huang, X. Zeng, L. Guo, J. Lan, L. Zhang and D. Cao, Heavy metal ion removal of wastewater by zeolite-imidazolate frameworks, *Sep. Purif. Technol.*, 2018, **194**, 462–469.

46 E. E. Jasper, V. O. Ajibola and J. C. Onwuka, Nonlinear regression analysis of the sorption of crystal violet and methylene blue from aqueous solutions onto an agro-waste derived activated carbon, *Appl. Water Sci.*, 2020, **10**(6), 1–11.

47 F. Dawodu, G. Akpomie and M. Abuh, Equilibrium Isotherm Studies on the Batch Sorption of Copper (II) ions from Aqueous Solution unto Nsu Clay, *Int. J. Appl. Sci. Eng. Res.*, 2012, **3**(12), 1–7.

48 X. Yang, J. Wang, A. M. El-Sherbeeny, A. A. AlHammadi, W. H. Park and M. R. Abukhadra, Insight into the adsorption and oxidation activity of a ZnO/piezoelectric quartz core-shell for enhanced decontamination of ibuprofen: steric, energetic, and oxidation studies, *Chem. Eng. J.*, 2022, **431**, 134312.

49 L. Sellaoui, H. Guedidi, L. Reinert, S. Knani, L. Duclaux and A. B. Lamine, Experimental and theoretical studies of adsorption of ibuprofen on raw and two chemically modified activated carbons: new physicochemical interpretations, *RSC Adv.*, 2016, **6**(15), 12363–12373.

50 R. A. Ali, M. Mobarak, A. M. Badawy, E. C. Lima, M. K. Seliem and H. S. Ramadan, New insights into the surface oxidation role in enhancing Congo red dye uptake by Egyptian ilmenite ore: experiments and physicochemical interpretations, *Surf. Interface*, 2021, **26**, 101316.

51 M. R. Abukhadra, N. M. Refay, A. M. El-Sherbeeny and M. A. El-Meligy, Insight into the loading and release properties of MCM-48/biopolymer composites as carriers for 5-fluorouracil: equilibrium modeling and pharmacokinetic studies, *ACS Omega*, 2020, **5**(20), 11745–11755.

52 M. Mostafa, M. A. El-Meligy, M. Sharaf, A. T. Soliman and M. R. AbuKhadra, Insight into chitosan/zeolite-A nanocomposite as an advanced carrier for levofloxacin and its anti-inflammatory properties; loading, release, and anti-inflammatory studies, *Int. J. Biol. Macromol.*, 2021, **179**, 206–216.

53 D. Tan, P. Yuan, F. Dong, H. He, S. Sun and Z. Liu, Selective loading of 5-fluorouracil in the interlayer space of methoxy-modified kaolinite for controlled release, *Appl. Clay Sci.*, 2018, **159**, 102–106.

54 F. Rehman, K. Ahmed, A. Rahim, N. Muhammad, S. Tariq, U. Azhar, A. J. Khan, Z. Sama, P. L. Volpe and C. Airoldi, Organo-bridged silsesquioxane incorporated mesoporous silica as a carrier for the controlled delivery of ibuprofen and fluorouracil, *J. Mol. Liq.*, 2018, **258**, 319–326.

55 M. Ge, W. Tang, M. Du, G. Liang, G. Hu and S. J. Alam, Research on 5-fluorouracil as a drug carrier materials with its in vitro release properties on organic modified magadiite, *Eur. J. Pharm. Sci.*, 2019, **130**, 44–53.

56 S. M. Ibrahim, M. N. Bin Jumah, S. I. Othman, R. S. Alruhaimi, N. Al-Khalawi, Y. F. Salama, A. A. Allam and M. R. Abukhadra, Synthesis of Chitosan/Diatomite Composite as an Advanced Delivery System for Ibuprofen Drug; Equilibrium Studies and the Release Profile, *ACS Omega*, 2021, **6**(20), 13406–13416.

57 H. El-Hamshary, M. H. El-Newehy, M. Moydeen Abdulhameed, A. ElFaham and A. S. Elsherbiny, Evaluation of clay-ionene nanocomposite carriers for controlled drug delivery: synthesis, in vitro drug release, and kinetics, *Mater. Chem. Phys.*, 2019, **225**, 122–132.